

pubs.acs.org/EF Communication

Impact of a Novel Nickel-Based Catalyst and Phenyl-Acrylate-Based Anion-Exchange Membrane in a Direct Urea Fuel Cell

Jaesik Yoon,[†] Jung Min Kim,[†] Yi-hung Lin, Geoffrey M. Geise, Bryan S. Beckingham,* and Dong-Joo Kim*



Cite This: Energy Fuels 2024, 38, 12274–12281



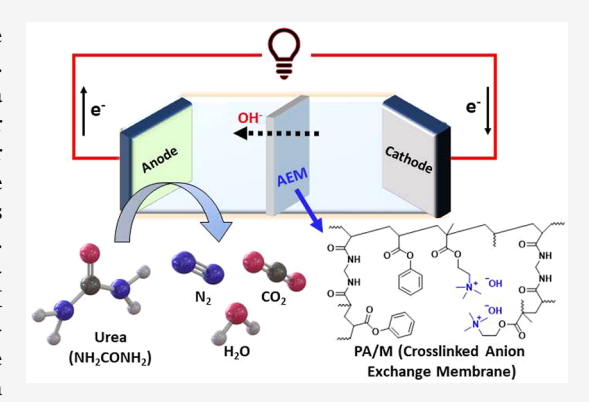
ACCESS I

III Metrics & More

Article Recommendations

s Supporting Information

ABSTRACT: Developing target-specific catalysts and anion-exchange membranes (AEMs) is crucial for direct urea fuel cell (DUFC) performance. To advance the DUFC system, we developed an anode catalyst with a nickel—iron oxyhydroxide/carbon (NiFeOOH/C) nanofibrous structure for the urea oxidation reaction (UOR), where we optimized the Ni/Fe molar ratio as 6:4. The enhanced electrocatalytic activity of the anode (Ni₆Fe₄OOH/C) is attributed to the hydroxide group, which responds with urea molecules to enhance the UOR in a pH-neutral system. Furthermore, we employed a recently developed cross-linked phenylacrylate-based AEM (PA/M). A DUFC prepared with the anode and PA/M generates a maximum power density of 11.1 mW/cm² and 0.92 V opencircuit voltage under 3 M urea as fuel at 25 °C. We further analyzed the applicability of PA/M in a DUFC system by measuring the urea partition coefficients and permeabilities over a range of concentrations.



Global environmental concerns demand the development of sustainable energy sources. Fuel cells and emerging hydrogen energy technologies require high-purity hydrogen production and low-cost catalyst materials. The direct urea fuel cell (DUFC) is an alternative energy platform that oxidizes urea to generate energy while offering compact size and high energy density operation at a low temperature. In comparison to the hydrogen production by water splitting (reversible potential of 1.23 V), the reversible potential of the urea oxidation reaction (UOR, 0.37 V) is significantly less. Moreover, DUFC technology efficiently converts energy from industrial and urinal wastewater containing urea to electrical power. A typical DUFC comprises a cathode, an anode, and an anion-exchange membrane (AEM); see Figure 1.

A DUFC operates by the UOR at the anode and the oxygen reduction reaction (ORR) at the cathode. At the anode, urea $[CO(NH_2)_2]$ and hydroxide (OH $^-$) are oxidized to water, nitrogen (N_2) , and carbon dioxide (CO_2) and generate electrons (e $^-$), where N_2 and CO_2 leave the system as gases. The excess e $^-$ are then transferred to the cathode to reduce O_2 and water (H_2O) to hydroxide (OH^-) . Finally, OH $^-$ is then permeated through an AEM to complete the loop (Figure 1). Thus, the DUFC performance can be improved by advancing the electrode reactivities (UOR and ORR) and the membrane selectivity to OH $^-$.

anode reaction

$$CO(NH_2)_2 + 6OH^- \rightarrow N_2 + CO_2 + 5H_2O + 6e^-$$

 $E = -0.746 \text{ V versus SHE}$ (1)

cathode reaction

$$O_2 + 4e^- + 2H_2O \rightarrow 4OH^ E = 0.4 \text{ V versus SHE}$$
 (2)

overall reaction

$$2CO(NH_2)_2 + 3O_2 \rightarrow 4H_2O + 2CO_2 + 2N_2$$

 $E = 1.146 \text{ V versus SHE}$ (3)

Nickel (Ni)-based catalysts have been considered for various electrochemical applications (e.g., supercapacitors, batteries, and DUFCs). 9-11 For systems such as DUFC, increasing the surface area of the catalyst is favorable to enhance the anode reactivity to the fuel (i.e., urea). In efforts to increase the anode surface area, a secondary metal (e.g., iron and Fe) has been considered to prepare an alloy or a composite-based catalyst. For instance, Ni/Fe-based catalysts offer a reduced onset

Received: February 28, 2024 Revised: June 14, 2024 Accepted: June 14, 2024 Published: June 25, 2024





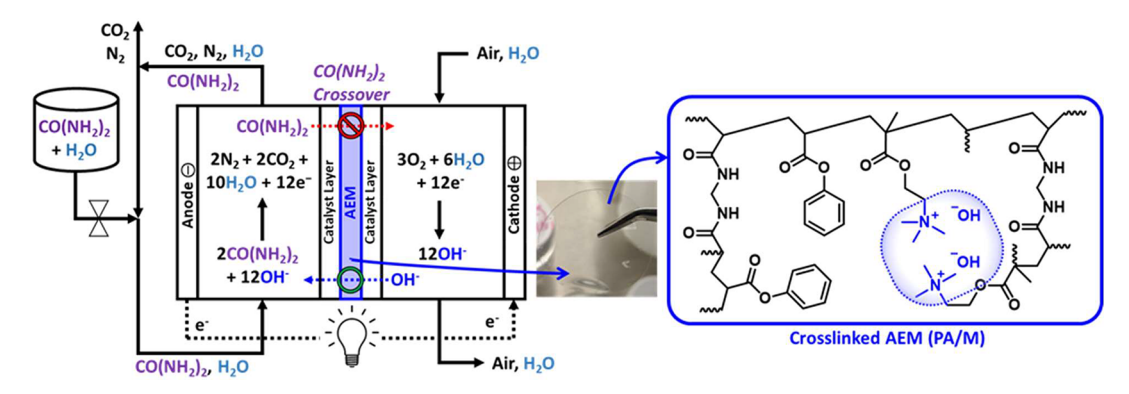


Figure 1. Schematic of a DUFC and the PA/M (cross-linked AEM) chemical structure.

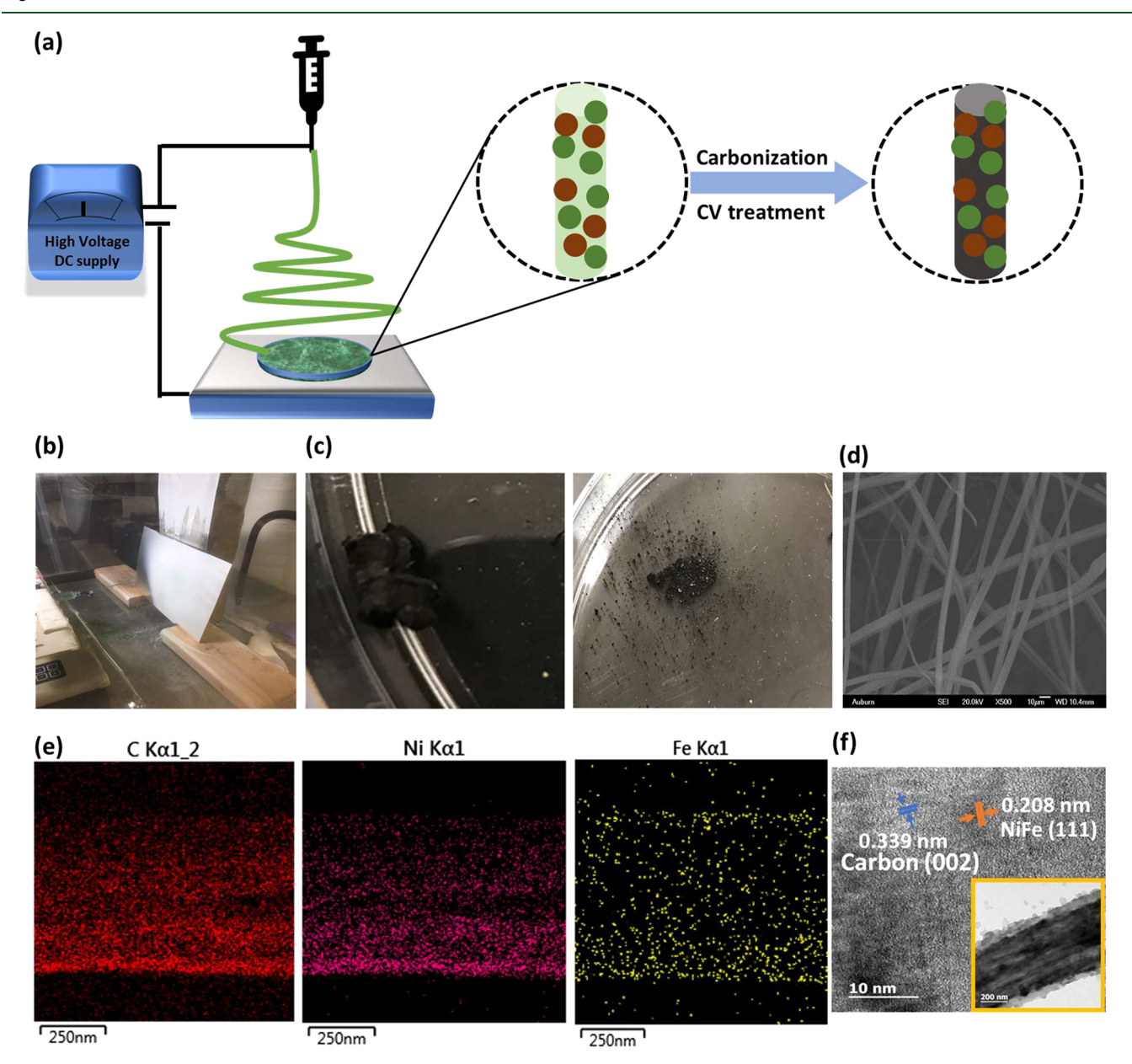


Figure 2. (a) Schematic illustration of the preparation procedures for NiFeOOH/C nanofibers, (b) syringe with a conductive outlet, (c) photos of washed and dried nanofiber, (d) SEM image of the nanofiber, (e) EDS mappings of the nanofiber to C, Ni, and Fe, and (f) TEM image of the nanofiber.

potential as Fe is being stabilized in high-valence Ni and introduces a greater surface area of the catalyst. ¹² While Ni/Fe

catalysts are relevant for basic environments, 13 they are not as suitable for pH-neutral conditions (agricultural and urinary

wastewater). Therefore, a current challenge in DUFC is to develop a catalyst that functions under pH-neutral conditions without pretreatments.

In this work, we introduced a nickel oxide hydroxide (NiOOH) catalyst by oxidizing nickel oxide/nickel hydroxide [NiO/Ni(OH)₂] simultaneously into nickel hydroxide (NiOOH) at a high potential (versus Hg/Hg₂O),¹⁴ resulting in the formation of active sites for the UOR in alkaline media.¹⁵ Lastly, we incorporated NiOOH with Fe (Ni-FeOOH) to avoid electrode blocking by surface-adsorbed CO species, improving the DUFC performance and stability.¹⁶

$$Ni(OH)_2 + OH^- \rightarrow NiOOH + H_2O + e^-$$
 (4)

$$6\text{NiOOH} + \text{CO(NH}_2)_2 + 6\text{OH}^-$$

 $\rightarrow 6\text{Ni(OH)}_2 + \text{CO}_2 + \text{N}_2 + 5\text{H}_2\text{O} + 6\text{e}^-$ (5

An AEM is a dense polymeric membrane with positive fixed charge groups (e.g., quaternary ammonium, 17 imidazolium, 18,19 etc.) that provide anion-selective transport. Transport of monatomic ions (e.g., Cl $^-$) $^{20-22}$ in AEMs has been well-studied, but transport of polyatomic ions (e.g., formate, 23 acetate, 23 and bicarbonate 17,24) or solutes (e.g., methanol, 25,26 ethanol, 23,25 and urea 27) has received less attention. One-dimensional Fickian analysis of solute transport through a membrane can be used to define the solute permeability (P_i) as the product of a sorption coefficient (K_i) and an average diffusion coefficient (D_i). $^{28-32}$

$$P_i = K_i D_i \tag{6}$$

The sorption (or partition) coefficient is sensitive to the affinity between the solute and the membrane.³³ For example, ion-containing polymeric membranes favor polar sorbates (alcohols³⁴ and urea) over nonpolar alkanes. The diffusion coefficient represents the kinetic component of the transport process and can be related to the diffusional jumps taken as the solute diffuses through the membrane.³⁵ Generally, the driving force of the solute transport is governed by the solute (e.g., urea and KOH) concentrations in both anode and cathode cells. Additionally, the electrochemical field (Nernst–Planck³⁶) contributes to the driving force of the charged ions (e.g., K⁺ and OH⁻).

Previously, Lan et al. performed a series of DUFC experiments with a linear polymer-based AEM prepared by blending 60 wt % styrene-divinylbenzene-based anion-exchange resin (AER, Amberlite IRA78) with 40 wt % poly(vinyl alcohol) (PVA, $M_{\rm w}$ of 50 000 g/mol).³⁷ They varied the urea concentration from 1 to 7 M in the feed (anode) cell and reported that the overall power density decreased as the urea concentration increased. This result indicates that the conduction of OH⁻ is the most critical (rate-determining) process. Therefore, the device efficacy may suffer from various factors (e.g., urea crossover) that lower the OH⁻ conductivity.

Cross-linked phenyl acrylate (PA)-based AEMs are promising membrane candidates for energy devices that are involved with polyatomic solutes (DUFC²⁷ and non-aqueous redox flow batteries³⁸). Recently, we reported the synthesis of a cross-linked AEM (PA/M) prepared with a cross-linker (N,N'-methylenebis(acrylamide), 30 mol %), a hydrophobic monomer (PA, 49 mol %), and a positively charged monomer (methacroylcholine chloride, 21 mol %) (Figure 1).²⁷ We then prepared membrane-electrode assemblies (MEAs) with a

conventional Ni-based catalyst (anode) and a silver catalyst (cathode) 15 to test the applicability of the PA/M in a DUFC at a dilute urea concentration (0.33 M) in the feed. At 50 °C, we acquired a power density of 3.4 mW/cm², higher than that (2.5 mW/cm²) from the setup with a conventional AEM (Fumasep FAA). We conjectured that the cross-links in PA/M may suppress the urea crossover by restricting polymer network swelling. 39,40

In this work, we aim to advance the DUFC system by introducing a NiFeOOH-based anode and a PA/M membrane. We characterized the anode with scanning electron microscopy (SEM) and transmission electron microscopy (TEM) and the PA/M membrane by measuring urea permeabilities $(P_{\rm u})^{41}$ and sorption coefficients $(K_{\rm u})^{28}$ at varied concentrations (0.33–3 M) and temperatures (25 and 55 °C). Lastly, we prepared MEA to measure the performance in a DUFC.

A series of NiFeOOH with carbon-nanofiber-based catalysts (NiFeOOH/C) were prepared by electrospinning (Figure 2a). The electrospinning approaches offer a versatile method to supply three-dimensional (3D) nanostructures to enhance the surface area of the nanofiber, urea transport, and e- transfer. First, NiFe/C was synthesized using the electrospinning method with carbonization. Polyvinylpyrrolidone (1.93 g), dissolved in dimethylformamide (15.0 mL), was added to water (5.0 mL) and ethanol (17.5 mL). Next, nickel(II) nitrate $[Ni(NO)_2]$ and iron(III) nitrate $[Fe(NO)_3]$ were added at various Ni/Fe molar ratios (100:0, 90:10, 80:20, 70:30, 60:40, and 50:50) and stirred for 5 h at room temperature. The resulting solution was loaded into a syringe with a conductive outlet and applied at a constant rate (0.50 mL/h and 20 kV), where the gap between the needle tip and flat aluminum foil was 10 cm (Figure 2b). The collected precursor nanofibers were carbonized at 950 °C for 5 h (heating rate of 3 °C/min at high-purity N₂ gas). Next, NiFe/C nanofiber was adopted as the working electrode in a cyclic voltammetry (CV) treatment containing 1 M KOH. NiFe/C was converted to NiFeOOH/C by CV treatment [between -0.1 and 0.6 V (versus Ag/AgCl)] for 10 cycles and then CV process at 0.6 V for 30 min to form an oxyhydroxide well. 42,43 Obtained NiFeOOH/C was washed and dried for 12 h at room temperature (Figure 2c). SEM was used to characterize the morphology of NiFeOOH/C. The SEM image confirms a uniform nanofibrous texture of the catalyst (Figure 2d).

While the high carbonization temperature slightly affects the density of nanofibrous structures, 44 3D nanofibrous structures still appeared to form NiFe/C catalysts after the carbonization process. The retention of the 3D nanofibrous morphology was observed, exposing potential active sites for UOR. The energydispersive spectroscopy (EDS) mapping of NiFeOOH/C suggested that relatively homogeneous C, Ni, and Fe dispersion was obtained through electrospinning, carbonization, and CV processes (Figure 2e). Among the series of nanofibers with varied Ni/Fe molar ratios, the nanofiber prepared with 60:40 Ni₆Fe₄OOH/C exhibited the highest current density with a low onset potential for UOR (Figure S1 of the Supporting Information). Therefore, Ni₆Fe₄OOH/C was selected for further characterization, unless noted. Additionally, atomic percentages of Ni₆Fe₄OOH/C were obtained from EDS analysis, shown in Table S1 of the Supporting Information. EDS mapping of TEM was used to investigate the detailed microstructure and alloy formation in Ni₆Fe₄OOH/C (Figure 2f). Consistent with the SEM image (Figure 2d), TEM images show bimetallic nanofibers with an

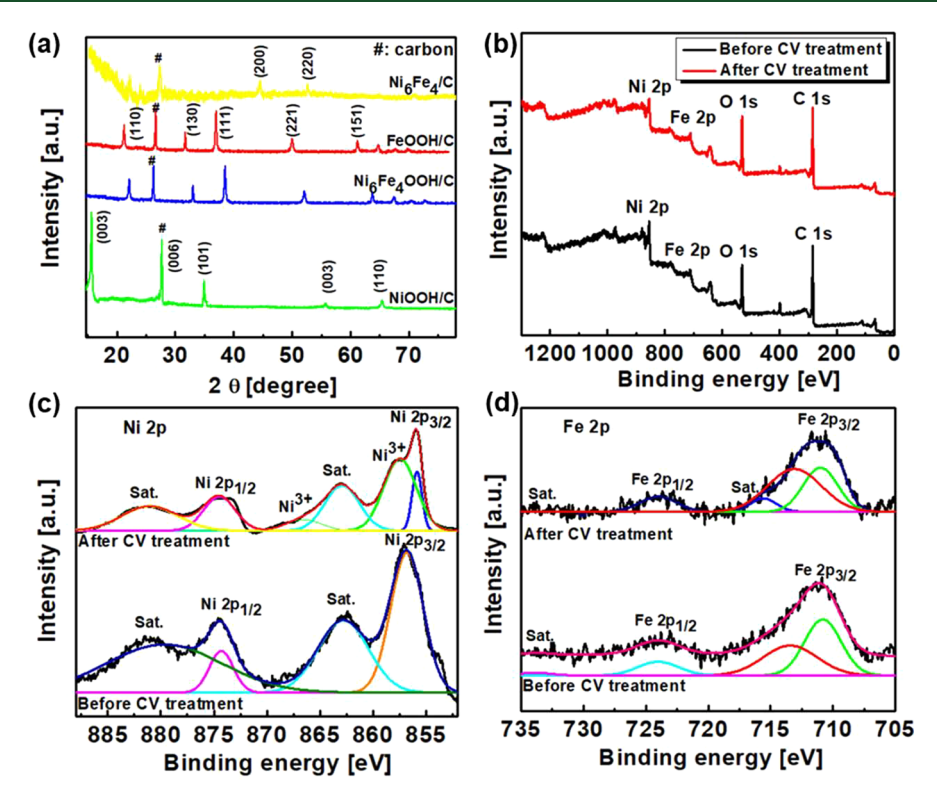


Figure 3. XRD spectra of (a) NiOOH/C, NiFeOOH/C, FeOOH/C, and NiFe/C and (b-d) X-ray photoelectron spectroscopy (XPS) spectra of Ni₆Fe₄/C (before CV treatment) and Ni₆Fe₄OOH/C (after CV treatment).

average diameter between 500 and 550 nm (Figure 2f). In addition, the TEM image depicted randomly dispersed carbon foam containing Ni and Fe on the electrode surface. A high-resolution TEM image was acquired, which shows the well-resolved parallel lattice fringes, and *d* spacings were measured to be 0.208 and 0.339 nm. It can be indexed to the (111) plane of the face-centered cubic (FCC) NiFe alloy and (002) plane of graphitic carbon, respectively. The selected area electron diffraction pattern of NiFeOOH/C describes the concentric rings formed by the occasional bright spot assigned to the (111), (200), (220), and (222) planes, which represent a polycrystalline FCC structure. Thus, the polycrystalline NiFeOOH/C nanofibers were confirmed, enhancing the active sites for UOR during the formation of the bimetallic composite. He

X-ray diffraction (XRD) of the prepared catalysts was carried out to examine the crystalline phases (Figure 3a). Ni₆Fe₄/C had two prominent diffraction peaks found at 44.7° and 51.8°, which are assigned to the (111) and (200) reflections of FCC NiFe alloys [Joint Committee on Powder Diffraction Standards (JCPDS) number 47-1417]. 45 The formation of NiFe alloys should be associated with the distinct carbon peaks (JCPDS number 41-1487),47 which are marked using "#" as a result of the decomposition of the polymer during the carbonization process. After CV treatment, oxyhydroxidebased compounds have emerged, such as NiOOH, FeOOH, and Ni₆Fe₄OOH. The diffraction peaks for NiOOH (JCPDS number 74-2075)⁴² and FeOOH (JCPDS number 29-0713)⁴⁸ are well-matched with their reference XRD patterns, respectively. The Ni₆Fe₄OOH/C nanofibers exhibit considerably similar diffraction peaks to those of FeOOH/C, implying that incorporated Ni may not change the crystal structure of FeOOH. Figure S2 of the Supporting Information

shows XRD patterns of as-CV-treated catalysts of NiFeOOH with different ratios of Ni/Fe, which are 9:1, 8:2, 7:3, and 6:4. The appearances, such as peak shifts, intensity changes, and peak broadening, would be remarked toward a 2θ angle with an increase in the Ni content at $38-40.5^{\circ}$. These results indicate the successful incorporation of Ni into the Fe structure, implying a decrease in the lattice parameter of Ni₆Fe₄OOH as a result of a lower lattice constant of Ni compared to Fe.

Panels b–d of Figure 3 present the Ni 2p spectra of Ni $_6$ Fe $_4$ /C before CV treatment, where two peaks were accompanied by two satellite peaks located at 863 eV (2p $_{3/2}$) and 880 eV (2p $_{1/2}$). ⁴⁹ The two nickel peaks at 857 and 875 eV correspond to Ni 2p $_{3/2}$ and Ni 2p $_{1/2}$, respectively ⁵⁰ (Figure 3c). However, the spectra of the CV-treated electrode exhibit a decrease in the satellite peaks and two extra peaks at 857 and 867 eV, ascribed to Ni $_6$ Fe $_4$ OOH/C. ⁴² These changes imply that complete conversion from Ni $_6$ Fe $_4$ /C to Ni $_6$ Fe $_4$ OOH/C was achieved.

Two broad peaks (at 711 and 724 eV) from the Fe 2p spectra of $\mathrm{Ni_6Fe_4/C}$ were deconvoluted by associating to the two spin—orbit doublets of Fe $2\mathrm{p_{3/2}}$ and Fe $2\mathrm{p_{1/2}}$, respectively (Figure 3d). Although these Fe 2p peaks are partially involved in an oxidation state of $\mathrm{Fe^{3^+}}$, after CV treatment, the distinguished position of the Fe $2\mathrm{p_{1/2}}$ component (712.0 eV) indicates the Fe³⁺ oxidation state. Besides, the Fe 2p peaks of $\mathrm{Ni_6Fe_4OOH/C}$ were accompanied by two small satellite peaks (at 718 and 733 eV) correlated to $\mathrm{Fe^{3^+}}$.

The electroactivity of Ni-based catalysts toward the UOR is enhanced when bimetallic alloys are employed as a result of the synergistic effect, ⁵² raising the Ni oxidation state ¹ and catalyst structure defect. ⁵³ In addition, the onset potential is moved to

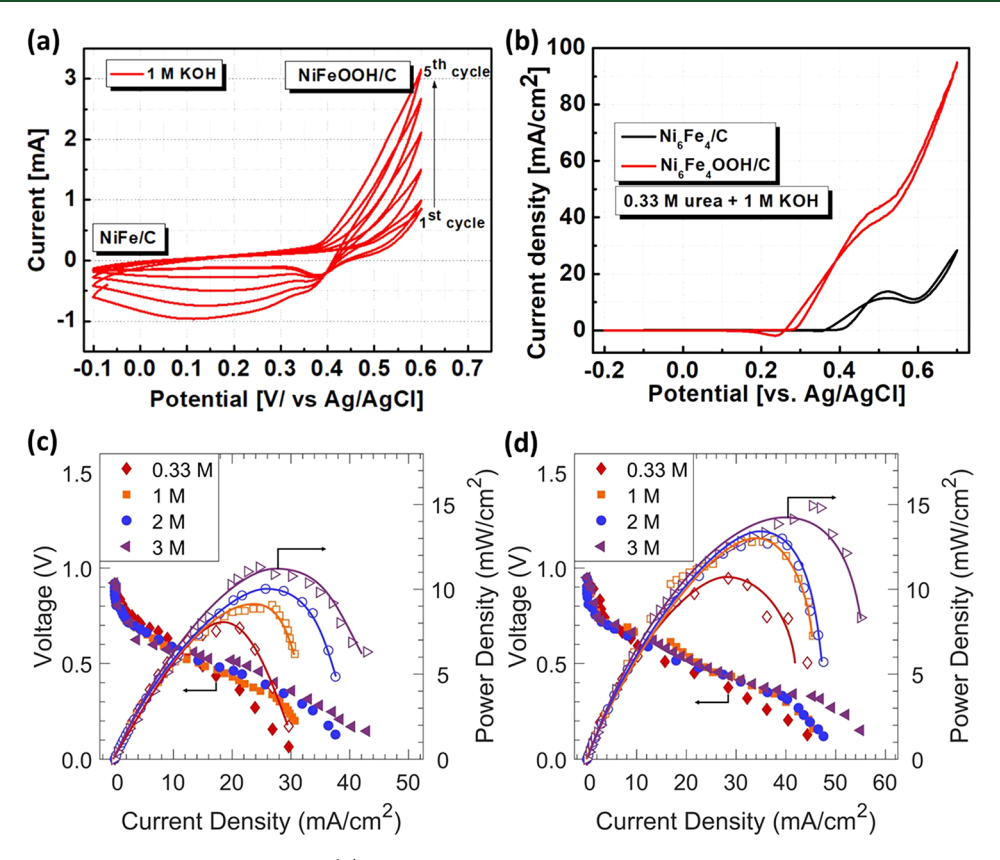


Figure 4. (a) CV results of urea oxidation for 5 cycles, (b) current densities to the potential for Ni_6Fe_4/C and $Ni_6Fe_4/OOH/C$ at 25 °C, and power densities and voltages of DUFC power densities under different urea concentrations at (c) 25 and (d) 55 °C, where lines are guides to the eye.

the negative potential owing to the redox potential of Fe²⁺/ Fe³⁺ being lower than the redox potential of Ni²⁺/Ni³⁺ for the UOR. The CV results of urea oxidation of the NiFe/C catalyst over 5 cycles in 1 M KOH solution are shown in Figure 4a. A couple of redox peaks are located between 0.38 and 0.55 V (versus Ag/AgCl) during the redox cycling, suggesting that the inclusion of OH⁻ induces the electrochemical conversion of NiFe/C to NiFeOOH/C.42 The current value rises as the number of CV cycles increases, implying that catalysts partially converted from NiFe to NiFeOOH. This phenomenon is attributed to catalyst activation, potentially encompassing the removal of surface contaminants, restructuring of the catalyst surface, or enhancement of electron transfer kinetics. The electroactivity of Ni-based catalysts toward the UOR is enhanced when bimetallic alloys are employed as a result of synergistic effects⁵² by enhancing the Ni oxidation state¹ and structural stability.⁵³ To achieve the optimal ratios of Ni/Fe (bare Ni to 5:5) for the UOR, we conducted CV tests at the same urea concentration in alkaline media (Figure S1 of the Supporting Information). In addition, the onset potential is moved to the negative potential owing to the redox potential of the Fe²⁺/Fe³⁺ couple being lower than Ni²⁺/Ni³⁺ for the UOR. Ni₆Fe₄OOH/C exhibits a prominent redox peak with anodic and cathodic peak potentials of 0.23 and 0.55 V (versus Ag/ AgCl) under an alkaline environment.

 Ni_6Fe_4OOH/C has a higher current density than that of Ni_6Fe_4/C at 0.33 M urea (with 1 M KOH at a scan rate of 10 mV/s) (Figure 4b). This result is likely due to Ni_6Fe_4OOH/C having more active sites to conduct the UOR. A higher current density in the forward scan leads to higher catalytic activity and resistance to byproduct poisoning. Moreover, the anodic peak of NiFe/C at 0.5 V (versus Ag/AgCl) was distinctly curved,

corresponding to the $\mathrm{Ni}^{2+}/\mathrm{Ni}^{3+}$ couple oxidation. On the other hand, the current densities of NiFeOOH/C increase gradually with the increase of potential as nickel oxide hydroxide formation (eq 4) is bypassed in the UOR. As we discussed, the electrochemical performance also depends upon limiting the urea crossover through the AEM. Here, we employed the cross-linked AEM (PA/M; see the Supporting Information for the synthetic approach) to suppress the urea permeation. To further study the catalytic durability of the $\mathrm{Ni}_6\mathrm{Fe}_4\mathrm{OOH/C}$ electrode, we conducted CV (Figure S3a of the Supporting Information) and chronoamperometry (CA) experiments (Figure S3b of the Supporting Information). The CV curves were almost unchanged during 200 cycles, and the CA result indicates a constant current density over 60 min, revealing the excellent stability of the $\mathrm{Ni}_6\mathrm{Fe}_4\mathrm{OOH/C}$ electrode.

Figure S4 of the Supporting Information displays the CVs of Ni₆Fe₄OOH/C and Ni₆Fe₄/C in real human urine at a scan rate of 10 mV s⁻¹. A similar UOR behavior was monitored in human urine with 0.33 M urea (a normal urea level in urine is 0.4–0.7 mol/day) at Ni₆Fe₄OOH/C, which can be measured through commercial measurement of the urea concentration (Figure S5 of the Supporting Information). In contrast, Ni₆Fe₄/C shows no distinct oxidation current density in the same solution, highlighting that the OH⁻ group is necessary to catalyze the UOR. Consequently, oxyhydroxide-based catalysts offer a unique platform for DUFC application with human urine as a source without any treatment.

Distinct from our previous work (where we cycled 0.33 M urea on the Ni(OH)₂/C anode at 20 and 50 °C),²⁷ we expanded the range of urea concentrations (0.33–3 M) on the NiFeOOH/C anode at 25 and 55 °C. Similar to our previous study, enhanced DUFC performance was observed at a higher

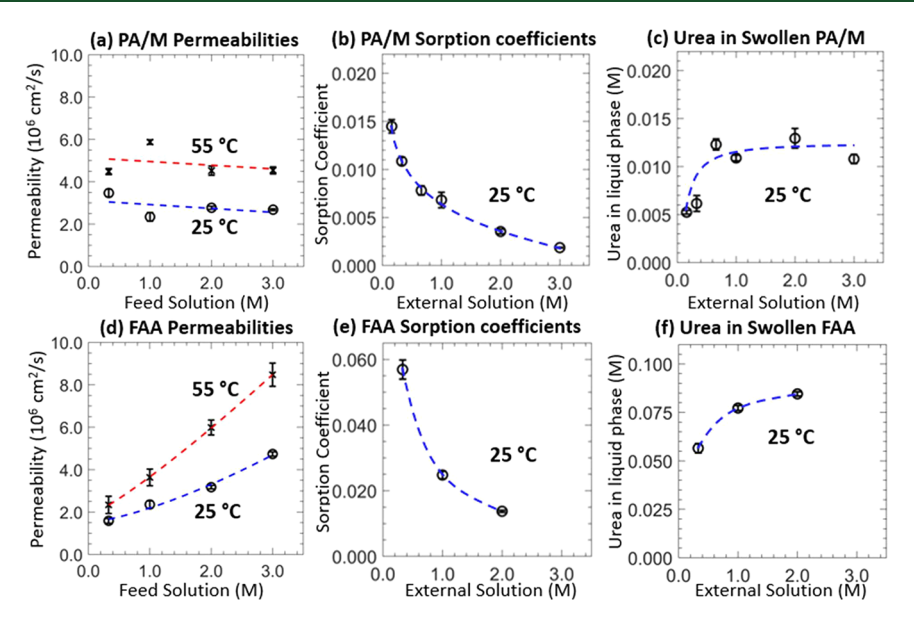


Figure 5. Membrane transport properties: urea permeabilities in (a) PA/M and (d) FAA at 25 and 55 °C, urea sorption coefficients in (b) PA/M and (e) FAA at 25 °C, and urea concentration in swollen (c) PA/M and (f) FAA after sorption experiments; see section S1.1 of the Supporting Information. All values were measured in triplicate, and the error bars indicate the standard deviation.

temperature (55 °C; panels c and d of Figure 4). This result suggests that UOR is favored at a higher temperature. In addition, we observed an increase in the maximum power density with higher urea concentrations. For instance, we received the maximum power densities of 11.08 and 14.15 mW/cm² with 0.92 and 0.99 open-circuit voltage (at 25 and 55 °C, respectively) at 3 M urea. This result is comparable to other DUFC setups prepared under similar conditions, ⁵⁴ as presented in Table S2 of the Supporting Information, which indicates that (1) both NiFeOOH/C (anode) and PA/M (membrane) are suitable for DUFC applications and (2) PA/M can be applicable in DUFC with more concentrated urea solutions (e.g., 5 M⁵⁵).

The urea permeabilities $(P_{\rm u})$ of PA/M were measured as a proxy to understand the degree of urea crossover during DUFC performance. $P_{\rm u}$ values were measured with a temperature-jacketed diffusion cell⁴⁰ over the range of 0.16–3 M upstream urea concentration at 25 and 55 °C (Figure 5a). We then compared the results to a linear AEM (Fumasep FAA) (Figure 5d). Generally, $P_{\rm u}$ values measured at 55 °C were higher than those measured at 25 °C. This result is due to diffusion being an activated process that expectedly increases diffusivity (and thus permeability) with an increasing temperature. As a result, the $P_{\rm u}$ values of the Fumasep FAA membrane increased with an increasing urea concentration (Figure 5d). In contrast, $P_{\rm u}$ values of PA/M did not increase over the same range of the concentration (Figure 5a).

The urea sorption coefficients $(K_{\rm u})$ were measured as a proxy to understand the affinity between the polymer and urea in water by sorption—desorption experiments²⁸ (panels b and e of Figure 5); see section S1.2 of the Supporting Information. Generally, the $K_{\rm u}$ values for both PA/M and FAA were decreased as the external urea concentration increases (panels b and e of Figure 5). These results are unexpected; for example, Galizia et al. reported constant sorption coefficients for linear polymer-based ion-exchange membranes (IEMs) and cross-linked membranes equilibrated with aqueous methanol (a polar organic sorbate³⁴) solutions between 0.1 and 12 M.²⁶ To further explain this unusual behavior, we estimated the urea

concentration within PA/M and FAA after being solvated in the external solutions (0.16-3 M urea) based on the solution volume fraction.²⁷ Apparently, the urea concentrations within both films (PA/M and FAA) did not increase after 0.012 and 0.085 M, respectively (panels c and f of Figure 5). A potential contribution to this unusual behavior is that mobile urea may form bivalent hydrogen bondings between polymer-bound hydrogen-bond acceptors (e.g., ketones on PA/M and sulfones on FAA⁵⁶) as the system reaches an equilibrium in urea sorption solutions.⁵⁷ As a result, a significant amount of urea may become less mobile and unable to diffuse out to the desorption solution (i.e., water).⁵⁸ To further investigate this potential adsorption, we employed a Fourier transform infrared (FTIR) spectrometer (Figure S6 of the Supporting Information). A urea peak (1161 cm⁻¹)²⁷ was detected from dried PA/ M films after sorption-desorption experiments. As a future work, a quantitative study is encouraged to capture the impact of urea within the polymer networks.

In summary, we introduced a novel NiFeOOH/C-based anode and studied the efficacy of PA/M (cross-linked AEM²⁷) in DUFC within a feed urea concentration range of 0.33–3 M at 25 and 55 °C. We measured the urea transport properties in PA/M with a non-cross-linked AEM (FAA). Here, we observed that the PA/M permeability to urea was consistent with urea concentrations when the FAA permeability to urea was increased (more urea crossover). We observed that urea sorption coefficients were low in both films. The sorption coefficients of PA/M were lower than those of FAA, indicating that less mobile urea is present in PA/M at an equilibrium. We observed that the maximum power density of DUFC becomes higher at a higher urea feed concentration, indicating that PA/M is stable at a higher concentration.

ASSOCIATED CONTENT

Supporting Information

The Supporting Information is available free of charge at https://pubs.acs.org/doi/10.1021/acs.energyfuels.4c00929.

Additional membrane preparation, experimental methods, and experimental results, including EDS, CV, XRD, comparsion table, and attenuated total reflectance (ATR)—FTIR spectroscopy (PDF)

AUTHOR INFORMATION

Corresponding Authors

Dong-Joo Kim — Materials Research and Education Center, Auburn University, Auburn, Alabama 36849, United States; orcid.org/0000-0001-5013-4005; Phone: +1-334-844-4864; Email: dkim@auburn.edu

Bryan S. Beckingham — Department of Chemical Engineering, Auburn University, Auburn, Alabama 36849, United States; orcid.org/0000-0003-4004-0755; Phone: +1-334-844-2036; Email: bsb0025@auburn.edu

Authors

Jaesik Yoon — Materials Research and Education Center, Auburn University, Auburn, Alabama 36849, United States Jung Min Kim — Department of Chemical Engineering, Auburn University, Auburn, Alabama 36849, United States; Department of Chemical Engineering, University of Virginia, Charlottesville, Virginia 22903, United States

Yi-hung Lin − Department of Chemical Engineering, Auburn University, Auburn, Alabama 36849, United States;
ocid.org/0000-0001-9025-153X

Geoffrey M. Geise — Department of Chemical Engineering, University of Virginia, Charlottesville, Virginia 22903, United States; orcid.org/0000-0002-5439-272X

Complete contact information is available at: https://pubs.acs.org/10.1021/acs.energyfuels.4c00929

Author Contributions

[†]Jaesik Yoon and Jung Min Kim contributed equally to this work.

Notes

The authors declare no competing financial interest.

ACKNOWLEDGMENTS

This material is based on work supported, in part, by the National Science Foundation under Grant CBET-1947936. This material is based on work supported, in part, by the U.S. Department of Energy, Office of Science, Office of Basic Energy Sciences, under Award DE-SC0021215. Any opinions, findings, and conclusions or recommendations expressed in this material are those of the authors and do not necessarily reflect the views of the National Science Foundation or U.S. Department of Energy.

■ REFERENCES

- (1) Sayed, E. T.; Eisa, T.; Mohamed, H. O.; Abdelkareem, M. A.; Allagui, A.; Alawadhi, H.; Chae, K.-J. Direct Urea Fuel Cells: Challenges and Opportunities. *J. Power Sources* **2019**, *417*, 159–175.
- (2) Asif, M.; Muneer, T. Energy Supply, Its Demand and Security Issues for Developed and Emerging Economies. *Renewable Sustainable Energy Rev.* **2007**, *11* (7), 1388–1413.
- (3) Kakati, N.; Li, G.; Chuang, P.-Y. A. Insights into the Ni/C-Based Thin-Film Catalyst Layer Design for Urea Oxidation Reaction in a Three-Electrode System. ACS Appl. Energy Mater. 2021, 4 (4), 4224–4233.
- (4) Boggs, B. K.; King, R. L.; Botte, G. G. Urea Electrolysis: Direct Hydrogen Production from Urine. *Chem. Commun.* **2009**, *0* (32), 4859–4861.

- (5) Senthilkumar, N.; Gnana Kumar, G.; Manthiram, A. 3D Hierarchical Core—Shell Nanostructured Arrays on Carbon Fibers as Catalysts for Direct Urea Fuel Cells. *Adv. Energy Mater.* **2018**, 8 (6), 1702207.
- (6) Yoon, J.; Lee, D.; Lee, Y. N.; Yoon, Y. S.; Kim, D.-J. Solid Solution Palladium-Nickel Bimetallic Anode Catalysts by Co-Sputtering for Direct Urea Fuel Cells (DUFC). *J. Power Sources* **2019**, 431, 259–264.
- (7) Wang, Y.; Liu, G. Reduced Graphene Oxide Supported Nickel Tungstate Nano-Composite Electrocatalyst for Anodic Urea Oxidation Reaction in Direct Urea Fuel Cell. *Int. J. Hydrogen Energy* **2020**, 45 (58), 33500–33511.
- (8) Urbańczyk, E.; Maciej, A.; Stolarczyk, A.; Basiaga, M.; Simka, W. The Electrocatalytic Oxidation of Urea on Nickel-Graphene and Nickel-Graphene Oxide Composite Electrodes. *Electrochim. Acta* **2019**, *305*, 256–263.
- (9) Yuan, C.; Sun, Z.; Jiang, Y.; Yang, Z.; Jiang, N.; Zhao, Z.; Qazi, U. Y.; Zhang, W.; Xu, A. One Step In Situ Growth of Iron-Nickel Sulfide Nanosheets on FeNi Alloy Foils: High Performance and Self Supported Electrodes for Water Oxidation. *Small* **2017**, *13* (18), 1604161.
- (10) Luo, J.; Im, J.-H.; Mayer, M. T.; Schreier, M.; Nazeeruddin, M. K.; Park, N.-G.; Tilley, S. D.; Fan, H. J.; Grätzel, M. Water Photolysis at 12.3% Efficiency via Perovskite Photovoltaics and Earth-Abundant Catalysts. *Science* **2014**, *345* (6204), 1593–1596.
- (11) Hu, F.; Zhu, S.; Chen, S.; Li, Y.; Ma, L.; Wu, T.; Zhang, Y.; Wang, C.; Liu, C.; Yang, X.; Song, L.; Yang, X.; Xiong, Y. Amorphous Metallic NiFeP: A Conductive Bulk Material Achieving High Activity for Oxygen Evolution Reaction in Both Alkaline and Acidic Media. *Adv. Mater.* 2017, 29 (32), 1606570.
- (12) Trotochaud, L.; Young, S. L.; Ranney, J. K.; Boettcher, S. W. Nickel-Iron Oxyhydroxide Oxygen-Evolution Electrocatalysts: The Role of Intentional and Incidental Iron Incorporation. *J. Am. Chem. Soc.* **2014**, *136* (18), *6744*–*6753*.
- (13) Ye, K.; Wang, G.; Cao, D.; Wang, G. Recent Advances in the Electro-Oxidation of Urea for Direct Urea Fuel Cell and Urea Electrolysis. *Top. Curr. Chem.* **2018**, 376 (6), 42.
- (14) Vedharathinam, V.; Botte, G. G. Direct Evidence of the Mechanism for the Electro-Oxidation of Urea on Ni(OH)₂ Catalyst in Alkaline Medium. *Electrochim. Acta* **2013**, *108*, 660–665.
- (15) Yoon, J.; Yoon, Y. S.; Kim, D.-J. Silver-Nanoparticle-Decorated NiOOH Nanorods for Electrocatalytic Urea Sensing. *ACS Appl. Nano Mater.* **2020**, 3 (8), 7651–7658.
- (16) Wang, L.; Li, M.; Huang, Z.; Li, Y.; Qi, S.; Yi, C.; Yang, B. Ni-WC/C Nanocluster Catalysts for Urea Electrooxidation. *J. Power Sources* **2014**, 264, 282–289.
- (17) Geise, G. M.; Hickner, M. A.; Logan, B. E. Ammonium Bicarbonate Transport in Anion Exchange Membranes for Salinity Gradient Energy. *ACS Macro Lett.* **2013**, *2* (9), 814–817.
- (18) Carter, B. M.; Keller, L.; Wessling, M.; Miller, D. J. Preparation and Characterization of Crosslinked Poly(Vinylimidazolium) Anion Exchange Membranes for Artificial Photosynthesis. *J. Mater. Chem. A* **2019**, 7 (41), 23818–23829.
- (19) Krödel, M.; Carter, B. M.; Rall, D.; Lohaus, J.; Wessling, M.; Miller, D. J. Rational Design of Ion Exchange Membrane Material Properties Limits the Crossover of CO₂ Reduction Products in Artificial Photosynthesis Devices. ACS Appl. Mater. Interfaces 2020, 12 (10), 12030–12042.
- (20) Geise, G.; Hickner, M.; Logan, B. Ionic Resistance and Permselectivity Tradeoffs in Anion Exchange Membranes. *ACS Appl. Mater. Interfaces* **2013**, *5* (20), 10294–10301.
- (21) Kamcev, J.; Paul, D. R.; Freeman, B. D. Effect of Fixed Charge Group Concentration on Equilibrium Ion Sorption in Ion Exchange Membranes. *J. Mater. Chem. A* **2017**, *5* (9), 4638–4650.
- (22) Kamcev, J.; Paul, D. R.; Manning, G. S.; Freeman, B. D. Predicting Salt Permeability Coefficients in Highly Swollen, Highly Charged Ion Exchange Membranes. *ACS Appl. Mater. Interfaces* **2017**, 9 (4), 4044–4056.

- (23) Kim, J. M.; Lin, Y.; Hunter, B.; Beckingham, B. S. Transport and Co-Transport of Carboxylate Ions and Ethanol in Anion Exchange Membranes. *Polymers* **2021**, *13* (17), 2885.
- (24) Dischinger, S. M.; Gupta, S.; Carter, B. M.; Miller, D. J. Transport of Neutral and Charged Solutes in Imidazolium-Functionalized Poly(Phenylene Oxide) Membranes for Artificial Photosynthesis. *Ind. Eng. Chem. Res.* **2020**, *59* (12), 5257–5266.
- (25) Carter, B. M.; Dobyns, B. M.; Beckingham, B. S.; Miller, D. J. Multicomponent Transport of Alcohols in an Anion Exchange Membrane Measured by *In-Situ* ATR FTIR Spectroscopy. *Polymer* **2017**, *123*, 144–152.
- (26) Galizia, M.; Paul, D. R.; Freeman, B. D. Liquid Methanol Sorption, Diffusion and Permeation in Charged and Uncharged Polymers. *Polymer* **2016**, *102*, 281–291.
- (27) Kim, J. M.; Wang, Y.; Lin, Y.; Yoon, J.; Huang, T.; Kim, D.-J.; Auad, M. L.; Beckingham, B. S. Fabrication and Characterization of Cross-Linked Phenyl-Acrylate-Based Ion Exchange Membranes and Performance in a Direct Urea Fuel Cell. *Ind. Eng. Chem. Res.* **2021**, *60* (41), 14856–14867.
- (28) Geise, G. M.; Falcon, L. P.; Freeman, B. D.; Paul, D. R. Sodium Chloride Sorption in Sulfonated Polymers for Membrane Applications. *J. Membr. Sci.* **2012**, 423, 195–208.
- (29) Geise, G. M.; Freeman, B. D.; Paul, D. R. Sodium Chloride Diffusion in Sulfonated Polymers for Membrane Applications. *J. Membr. Sci.* **2013**, 427, 186–196.
- (30) Hallinan, D. T.; Elabd, Y. A. Diffusion and Sorption of Methanol and Water in Nafion Using Time-Resolved Fourier Transform Infrared-Attenuated Total Reflectance Spectroscopy. *J. Phys. Chem. B* **2007**, *111* (46), 13221–13230.
- (31) Wijmans, J. G.; Baker, R. W. The Solution-Diffusion Model: A Review. J. Membr. Sci. 1995, 107 (1-2), 1-21.
- (32) Hegde, V. H.; Doherty, M. F.; Squires, T. M. A Two-Phase Model That Unifies and Extends the Classical Models of Membrane Transport. *Science* **2022**, *377* (6602), 186–191.
- (33) Afanas'ev, V. N. Solvation of Electrolytes and Nonelectrolytes in Aqueous Solutions. *J. Phys. Chem. B* **2011**, *115* (20), 6541–6563.
- (34) Katzenberg, A.; Angulo, A.; Kusoglu, A.; Modestino, M. A. Impacts of Organic Sorbates on the Ionic Conductivity and Nanostructure of Perfluorinated Sulfonic-Acid Ionomers. *Macromolecules* **2021**, 54 (11), 5187–5195.
- (35) Wei, C.; Yu, W.; Liang, X.; Zhang, Y.; Zhang, F.; Song, W.; Ge, X.; Wu, L.; Xu, T. Host—Guest Interaction Induced Ion Channels for Accelerated OH- Transport in Anion Exchange Membranes. *J. Membr. Sci.* **2022**, *655*, 120580.
- (36) Brumleve, T. R.; Buck, R. P. Numerical Solution of the Nernst-Planck and Poisson Equation System with Applications to Membrane Electrochemistry and Solid State Physics. *J. Electroanal. Chem. Interfacial Electrochem.* **1978**, 90 (1), 1–31.
- (37) Lan, R.; Tao, S.; Irvine, J. T. S. A Direct Urea Fuel Cell—Power from Fertiliser and Waste. *Energ Environ. Sci.* **2010**, 3 (4), 438–441.
- (38) Mazumder, Md. M. R.; Jadhav, R. G.; Minteer, S. D. Phenyl Acrylate-Based Cross-Linked Anion Exchange Membranes for Non-Aqueous Redox Flow Batteries. *ACS Mater. Au* **2023**, 3 (5), 557–568.
- (39) Jang, E.-S.; Kamcev, J.; Kobayashi, K.; Yan, N.; Sujanani, R.; Dilenschneider, T. J.; Park, H. B.; Paul, D. R.; Freeman, B. D. Influence of Water Content on Alkali Metal Chloride Transport in Cross-Linked Poly(Ethylene Glycol) Diacrylate. 2. Ion Diffusion. *Polymer* 2020, 192, 122316.
- (40) Dobyns, B. M.; Kim, J. M.; Beckingham, B. S. Multicomponent Transport of Methanol and Sodium Acetate in Poly(Ethylene Glycol) Diacrylate Membranes of Varied Fractional Free Volume. *Eur. Polym. J.* **2020**, *134*, 109809.
- (41) Beckingham, B. S.; Lynd, N. A.; Miller, D. J. Monitoring Multicomponent Transport Using *in Situ* ATR FTIR Spectroscopy. *J. Membr. Sci.* **2018**, *550*, 348–356.
- (42) Hu, C.-W.; Yamada, Y.; Yoshimura, K. Fabrication of Nickel Oxyhydroxide/Palladium (NiOOH/Pd) Thin Films for Gasochromic Application. *J. Mater. Chem. C* **2016**, 4 (23), 5390–5397.

- (43) Kudo, A.; Miseki, Y. Heterogeneous Photocatalyst Materials for Water Splitting. *Chem. Soc. Rev.* **2009**, 38 (1), 253–278.
- (44) Pampal, E. S.; Stojanovska, E.; Simon, B.; Kilic, A. A Review of Nanofibrous Structures in Lithium Ion Batteries. *J. Power Sources* **2015**, *300*, 199–215.
- (45) Kumar, A.; Chaudhary, D. K.; Parvin, S.; Bhattacharyya, S. High Performance Duckweed-Derived Carbon Support to Anchor NiFe Electrocatalysts for Efficient Solar Energy Driven Water Splitting. *J. Mater. Chem. A* **2018**, *6* (39), 18948–18959.
- (46) Lan, R.; Tao, S. Preparation of Nano-Sized Nickel as Anode Catalyst for Direct Urea and Urine Fuel Cells. *J. Power Sources* **2011**, 196 (11), 5021–5026.
- (47) Zhang, G.; Zhu, J.; Zeng, W.; Hou, S.; Gong, F.; Li, F.; LI, C. C.; Duan, H. Tin Quantum Dots Embedded in Nitrogen-Doped Carbon Nanofibers as Excellent Anode for Lithium-Ion Batteries. *Nano Energy* **2014**, *9*, 61–70.
- (48) Suryawanshi, M. P.; Shin, S. W.; Ghorpade, U. V.; Kim, J.; Jeong, H. W.; Kang, S. H.; Kim, J. H. A Facile, One-Step Electroless Deposition of NiFeOOH Nanosheets onto Photoanodes for Highly Durable and Efficient Solar Water Oxidation. *J. Mater. Chem. A* **2018**, 6 (42), 20678–20685.
- (49) Modak, A.; Mohan, R.; Rajavelu, K.; Cahan, R.; Bendikov, T.; Schechter, A. Metal—Organic Polymer-Derived Interconnected Fe-Ni Alloy by Carbon Nanotubes as an Advanced Design of Urea Oxidation Catalysts. ACS Appl. Mater. Interfaces 2021, 13 (7), 8461—8473.
- (50) Sun, H.; Zhang, W.; Li, J.-G.; Li, Z.; Ao, X.; Xue, K.-H.; Ostrikov, K. K.; Tang, J.; Wang, C. Rh-Engineered Ultrathin NiFe-LDH Nanosheets Enable Highly-Efficient Overall Water Splitting and Urea Electrolysis. *Appl. Catal.*, B **2021**, 284, 119740.
- (51) Yang, T.; Meng, L.; Han, S.; Hou, J.; Wang, S.; Wang, X. Simultaneous Reductive and Sorptive Removal of Cr(vi) by Activated Carbon Supported β -FeOOH. RSC Adv. **2017**, 7 (55), 34687–34693.
- (52) Song, F.; Zhu, Q.; Yang, X.; Zhan, W.; Pachfule, P.; Tsumori, N.; Xu, Q. Metal—Organic Framework Templated Porous Carbon Metal Oxide/Reduced Graphene Oxide as Superior Support of Bimetallic Nanoparticles for Efficient Hydrogen Generation from Formic Acid. *Adv. Energy Mater.* **2018**, 8 (1), 1701416.
- (53) Kim, J.-W.; Park, S.-M. In Situ XANES Studies of Electrodeposited Nickel Oxide Films with Metal Additives for the Electro-Oxidation of Ethanol. *J. Electrochem. Soc.* **2003**, *150* (11), E560– E566.
- (54) Gnana Kumar, G.; Farithkhan, A.; Manthiram, A. Direct Urea Fuel Cells: Recent Progress and Critical Challenges of Urea Oxidation Electrocatalysis. *Adv. Energy Sustainable Res.* **2020**, *1* (1), 2000015.
- (55) Zhang, H.; Wang, Y.; Wu, Z.; Leung, D. Y. C. A Direct Urea Microfluidic Fuel Cell with Flow-through Ni-Supported-Carbon-Nanotube-Coated Sponge as Porous Electrode. *J. Power Sources* **2017**, 363, 61–69.
- (56) Lo Vecchio, C.; Carbone, A.; Gatto, I.; Baglio, V. Investigation of Fumasep® FAA3-50 Membranes in Alkaline Direct Methanol Fuel Cells. *Polymers* **2023**, *15* (6), 1555.
- (57) Sagle, L. B.; Zhang, Y.; Litosh, V. A.; Chen, X.; Cho, Y.; Cremer, P. S. Investigating the Hydrogen-Bonding Model of Urea Denaturation. *J. Am. Chem. Soc.* **2009**, *131* (26), 9304–9310.
- (58) Rodríguez-Ropero, F.; van der Vegt, N. F. A. On the Urea Induced Hydrophobic Collapse of a Water Soluble Polymer. *Phys. Chem. Chem. Phys.* **2015**, *17* (13), 8491–8498.